AIAA SciTech Forum
12-16 January 2026, Orlando, FL
AIAA SCITECH 2026 Forum

10.2514/6.2026-0475

IDDES Analysis of Flapped Coflow Jet Airfoil at Low Reynolds Numbers

Jaehyoung Jeon * and Gecheng Zha †
Dept. of Mechanical and Aerospace Engineering
University of Miami, Coral Gables, Florida 33124

Abstract

This paper investigates the flow physics of a flapped coflow jet (FCFJ) airfoil designed to achieve ultra-high cruise lift coefficients (C_L) at low Reynolds number conditions of the Martian atmosphere. The study aims to develop a fundamental understanding of how coflow jet active flow control achieves attached flow at low Reynolds number conditions, which is crucial for future Mars exploration missions that require efficient aerial vehicles. Computational fluid dynamics (CFD) simulations are conducted using a validated 3D Navier-Stokes solver incorporating the Improved Delayed Detached Eddy Simulation (IDDES) turbulence model, a fifth-order WENO scheme for inviscid fluxes, and second-order central differencing for viscous terms. The flow conditions are at Mach number of 0.17 and Reynolds number of 56,300 with a momentum coefficient C_μ of 0.25.

Results demonstrate that 2D RANS and 3D IDDES predictions exhibit similar lump performance parameters, but the IDDES reveals more detailed flow structures. Detailed component analysis using the turbulent wall jet momentum equation reveals distinct flow attachment mechanisms across the airfoil. Near the leading edge, the flow is primarily laminar and is driven by a favorable pressure gradient for flow attachment. In the injection region, the high-momentum jet introduces significant streamwise inertia force term, which becomes the critical factor for energizing the boundary layer and promoting mixing with the main flow. As the flow moves over the flap, turbulent diffusion emerges as the primary mechanism for mixing and maintaining flow attachment against the adverse pressure gradient, with streamwise inertia force remaining a key contributor. Finally, in the vicinity of the suction slot, the strong favorable pressure gradient generated by the micro-compressor actuator becomes the dominant force, effectively suppressing separation. The insights gained into the low Reynolds number flow physics and attachment mechanisms provide a robust foundation for the design of future Martian aerial vehicles.

Nomenclature

CFJ	CoFlow jet
$CFWJ$	CoFlow Wall jet
$EAPG$	Extreme Adverse Pressure Gradient
$FCFJ$	Flapped CoFlow jet

* Ph.D. Candidate
† Professor, ASME Fellow, AIAA associate Fellow

$AoA(\alpha)$	Angle of attack
β	Deflection angle
LE	Leading Edge
TE	Trailing Edge
D/H	Distance from the inner wall normalized by the injection slot height
s	Airfoil Span length
c	Profile chord
U	Flow velocity
q	Dynamic pressure $0.5\,\rho\,U^2$
p	Static pressure
T	Static temperatue
ρ	Air density
μ	Dynamic viscosity
R	Specific gas constant
P	Pumping power
C_L	Lift coefficient $L/(q_\infty\,S)$
C_D	Drag coefficient $D/(q_\infty\,S)$
C_μ	Jet momentum coef. $\dot{m}_j\,U_j/(q_\infty\,S)$
Pc	Power coefficient $P/(q_\infty\,S\,V_\infty)$
$(C_L/C_D)_c$	CFJ airfoil corrected efficiency $C_L/(C_D$+Pc)
R_e	Reynolds number
M	Mach number
c_p	Constant pressure specific heat
γ	Air specific heats ratio
S	Planform area of the airfoil
T_t	Total temperature
P_t	Total pressure
H_t	Total specific enthalpy
$IDDES$	Improved Delayed Detached Eddy Simulation
$\dot{m}$	Mass flow across the pump
$_\infty$	Subscript, stands for free stream
$_j$	Subscript, stands for jet

1 Introduction

The growing interest in Mars exploration necessitates technological advancements to enhance the mobility range of aerial robots on the Martian surface. However, the Martian environment presents unique challenges for atmospheric flight due to its thin atmosphere and diverse terrain. Addressing these challenges requires high-performance, high-efficiency aircraft specifically designed for Martian conditions to enable future exploration missions.

Such aircraft offer numerous advantages, including enhanced mobility and accessibility for exploring vast Martian landscapes, facilitating resource discovery, identifying the presence of water, ice, and methane, and enabling comprehensive studies of Martian geological history. A critical challenge in developing these aircraft lies in generating ultra-high lift coefficients to minimize vehicle size and weight in

the thin Martian atmosphere, which is characterized by low Reynolds numbers and low air density.

Mars possesses significantly lower atmospheric density, approximately 1/100 of the one on Earth, necessitating innovative aircraft technologies. While Earth-based aircraft rely on conventional air-airfoil interactions to generate lift, the tenuous Martian atmosphere poses a formidable challenge for achieving the necessary lift for sustained flight. Fixed wing Mars aircraft are preferred for their high efficiency if feasible. Potential conventional solutions include significantly larger airfoil areas, increased aspect ratios, reduced airfoil loading, and novel control surfaces specifically tailored to the Martian environment [1].

Active flow control (AFC) has emerged as a promising technology for improving aerodynamic performance at low Reynolds numbers, typically for increasing maximum lift coefficient (C_{Lmax}) by suppressing flow separation and enhancing airfoil circulation. This is achieved by adding energy to the flow, typically through techniques such as blowing or suction. However, implementing AFC for cruise conditions presents a bigger challenge. Unlike at high lift takeoff and landing phase that a high power require may be acceptable due to the short transient time, cruise performance on Mars requires a high lift coefficient and a high aerodynamic efficiency at the same time.

Recently, Zha et al [2] developed a Martian electric VTOL aircraft MAGGIE (Mars Aerial and Ground Global Intelligent Explorer) enabled by CoFlow Jet (CFJ) active flow control. The flapped CFJ (FCFJ) airfoil shown in Fig. 1 is adopted for MAGGIE's wings.

1.1 Flapped CoFlow Jet Airfoil

The concept of flapped coflow jet airfoil is adopted from the CFJ airfoil with deflected slipstream for VTOL aircraft develped by Zha et al. [3].

The CFJ is applied inside a long flap that is a part of the flapped CFJ airfoil, as shown in Fig.1 [4], which has the injection located at the shoulder of the flap. A regular CFJ airfoil applies the injection very close to the leading edge at a point of around 2-4% Chord location. A suction slot is located near the flap trailing edge. A small amount of flow is withdrawn through the suction slot, pressurized by a micro-compressor actuator system, and then ejected tangent to the airfoil surface via the injection slot. More detailed CFJ concept and development can be found in [5–20]. By deflecting the flap rather than rotating the front of the airfoil, the FCFJ airfoil has the advantage of allowing the airfoil to change the angle of attack and lift coefficient without tilting the airfoils or the aircraft. The purpose of this paper is to demonstrate numerically that the FCFJ airfoil is a promising candidate to provide ultra-high cruise lift coefficient for 3D airfoil that can be used in low Reynolds number conditions of Martian atmosphere.

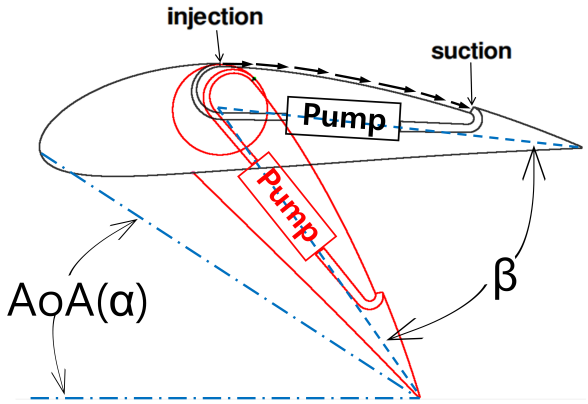

Figure 1: Sketch of flapped CFJ airfoil with the CoFlow jet applied on the flap

Compared to a 2D baseline airfoil, Wang and Zha [21] demonstrate that a 2D CFJ airfoil can achieve significantly higher cruise lift coefficients and aerodynamic efficiency, defined as:

$$\left(\frac{C_L}{C_D}\right)_c = \frac{C_L}{C_D + P_c} \tag{1}$$

To achieve high cruise efficiency, it is essential to maintain low CFJ power requirements, denoted by the CFJ required power coefficient, P_c.

To assess the transportation productivity of aircraft, a parameter encompassing both range and gross weight is introduced: cruise productivity efficiency. This metric, proposed by Yang et al. [16], provides a more comprehensive evaluation of aircraft performance, considering not only aerodynamic efficiency but also payload capacity and range capability:

$$\left(\frac{C_L^2}{C_D}\right)_c = \frac{C_L^2}{C_D + P_c} \tag{2}$$

CFJ airfoils can achieve substantially higher cruise C_L values and thus greater productivity efficiency. Taking advantage of the high cruise lift coefficient and resulting strong suction effect on the airfoil upper surface, Ren and Zha [22] designed a tandem airfoil aircraft configuration where the front airfoil tip vortex is captured by the rear airfoil to enhance overall system efficiency. However, for cruise conditions, the conventional CFJ configuration shown in Fig. 1 appears to experience rapid energy consumption increases when C_L exceeds 1.6 [16, 23]. Although the aerodynamic drag coefficient C_D can remain small and the pure aerodynamic lift-to-drag ratio C_L/C_D can still be very high, the corrected aerodynamic efficiency defined in Eq. (1) can decrease rapidly with increasing C_L.

The purpose of this study is to develop a high lift coefficient and high productivity efficiency airfoil for low Reynolds number conditions characteristic of Mars. These features will provide essential feasibility for Martian flight operations. The high productivity efficiency combined with high lift coefficient will enable a compact and lightweight vehicle with substantial payload capacity. Additionally, it will allow the aircraft to operate at lower speeds, thereby reducing propulsion power requirements, which scale with the cube of flight velocity.

Flapped CoFlow Jet technology has emerged as a promising solution for achieving high C_L while maintaining favorable $(C_L/C_D)_c$ values. This capability makes it particularly relevant for aircraft operating in low-density environments, such as at high altitudes on Earth or in the Martian atmosphere. As demonstrated in previous studies [4, 24], flapped CFJs can significantly enhance lift performance, creating opportunities for various flight applications.

Building upon these promising findings, the present study conducts a numerical investigation of 3D flapped CFJ airfoils under low Reynolds number conditions representative of the Martian atmosphere, with the objective of gaining fundamental physical understanding of how coflow jet technology can maintain superior performance at such low Reynolds number conditions.

Xu et al. [20, 25] simulated the widely studied NASA hump using 2D URANS, implementing a "Co-Flow Wall Jet" (CFWJ) to attach the flow in the hump's adverse pressure gradient. Xu et al. dissected the physical mechanisms responsible for offsetting the APG to maintain flow attachment, concluding that the injection jet mass flux, streamwise vorticity, and turbulent diffusion are the three factors responsible for offsetting the APG. In particular, turbulent diffusion plays a dominant role among the three factors.

McBreen et al [26, 27] conducted IDDES of a CFJ airfoil to investigate the extreme adverse pressure gradient (EAPG) effect. Their results are consistent with the findings of Xu et al [25] that turbulent diffusion is the main factor offsetting the EAPG and make the flow attached. However, all the previous results analyzing the CFJ mechanism to attach flows in APG are at high Reynolds numbers.

The purpose of this paper is to conduct Improved Delayed Detached Eddy Simulation (IDDES) to study the flow attachment mechanism in adverse pressure gradient at low Reynolds numbers. IDDES is a hybrid RANS/LES model evolved from the Detached Eddy Simulation (DES) model under a series of developments by Spalart et al. [28, 29]. IDDES resolves the non-isotropic large eddies outside of boundary layer by using LES, but adopts the RANS model within the wall boundary layer. It is thus still limited to the Boussinesq eddy viscosity assumption within the boundary layer. The turbulence behavior very near the wall may not be adequately resolved. However, 3D IDDES provides considerably more insight into the flow physics of CFJ flows than 2D UARNS, especially for understanding the Reynolds number effects on the flow control mechanisms. Previous studies indicate that the IDDES and DES predicts the massive separated flow with significantly improved accuracy over URANS quantitatively and qualitatively [30–35]. The investigation of low Reynolds number effects is crucial for understanding the fundamental physics of CFJ flow control and its applicability to various flight conditions and aircraft scales.

2 Methodology

The IDDES solver implemented and validated by Yang and Zha [31, 36] is adopted in this study.

2.1 Governing Equations

The spatially filtered Navier-Stokes governing equations in generalized coordinates are expressed as:

$$\frac{\partial Q}{\partial t}+\frac{\partial E}{\partial \xi}+\frac{\partial F}{\partial \eta}+\frac{\partial G}{\partial \zeta}=\frac{1}{Re}\left(\frac{\partial E_v}{\partial \xi}+\frac{\partial F_v}{\partial \eta}+\frac{\partial G_v}{\partial \zeta}+S\right) \tag{3}$$

where Re is the Reynolds number. The equations are normalized based on airfoil chord L_∞, freestream density ρ_∞ and velocity U_∞.

The conservative variable vector Q, the inviscid flux vectors E, F, G, the viscous flux E_v, F_v, G_v and the source term vector S are expressed as

$$Q = \frac{1}{J}\begin{pmatrix} \bar{\rho} \\ \bar{\rho}\tilde{u} \\ \bar{\rho}\tilde{v} \\ \bar{\rho}\tilde{w} \\ \bar{\rho}\tilde{e} \\ \bar{\rho}\tilde{\nu}_t \end{pmatrix}, \quad E = \begin{pmatrix} \bar{\rho}U \\ \bar{\rho}\tilde{u}U + l_x\bar{p} \\ \bar{\rho}\tilde{v}U + l_y\bar{p} \\ \bar{\rho}\tilde{w}U + l_z\bar{p} \\ (\bar{\rho}\tilde{e} + \bar{p})U - l_t\bar{p} \\ \bar{\rho}\tilde{\nu}U \end{pmatrix}, \quad F = \begin{pmatrix} \bar{\rho}V \\ \bar{\rho}\tilde{u}V + m_x\bar{p} \\ \bar{\rho}\tilde{v}V + m_y\bar{p} \\ \bar{\rho}\tilde{w}V + m_z\bar{p} \\ (\bar{\rho}\tilde{e} + \bar{p})V - m_t\bar{p} \\ \bar{\rho}\tilde{\nu}V \end{pmatrix}, \quad G = \begin{pmatrix} \bar{\rho}W \\ \bar{\rho}\tilde{u}W + n_x\bar{p} \\ \bar{\rho}\tilde{v}W + n_y\bar{p} \\ \bar{\rho}\tilde{w}W + n_z\bar{p} \\ (\bar{\rho}\tilde{e} + \bar{p})W - n_t\bar{p} \\ \bar{\rho}\tilde{\nu}W \end{pmatrix} \tag{4}$$

$$E_v = \begin{pmatrix} 0 \\ l_k\bar{\tau}_{xk} \\ l_k\bar{\tau}_{yk} \\ l_k\bar{\tau}_{zk} \\ l_k(\tilde{u}_i\bar{\tau}_{ki} - \bar{q}_k) \\ \frac{\bar{\rho}}{\sigma}(\nu + \tilde{\nu})(l \cdot \nabla\tilde{\nu}) \end{pmatrix}, \quad F_v = \begin{pmatrix} 0 \\ m_k\bar{\tau}_{xk} \\ m_k\bar{\tau}_{yk} \\ m_k\bar{\tau}_{zk} \\ m_k(\tilde{u}_i\bar{\tau}_{ki} - \bar{q}_k) \\ \frac{\bar{\rho}}{\sigma}(\nu + \tilde{\nu})(m \cdot \nabla\tilde{\nu}) \end{pmatrix}, \quad G_v = \begin{pmatrix} 0 \\ n_k\bar{\tau}_{xk} \\ n_k\bar{\tau}_{yk} \\ n_k\bar{\tau}_{zk} \\ n_k(\tilde{u}_i\bar{\tau}_{ki} - \bar{q}_k) \\ \frac{\bar{\rho}}{\sigma}(\nu + \tilde{\nu})(n \cdot \nabla\tilde{\nu}) \end{pmatrix} \tag{5}$$

$$S = \frac{1}{J}\begin{pmatrix} 0 \\ 0 \\ 0 \\ 0 \\ 0 \\ S_\nu \end{pmatrix} \tag{6}$$

where ρ is the density, p is the static pressure, and e is the total energy per unit mass. The overbar denotes a regular filtered variable in the LES region, or a Reynolds-averaged value in the RANS region. The tilde symbol is used to denote Favre filtered variables. ν is kinematic viscosity and $\tilde{\nu}$ is the working variable related to eddy viscosity in the S-A and IDDES turbulence one equation model [28, 29]. U, V and W are the contravariant velocities in ξ, η, ζ directions, and defined as

$$U = l_t + l \cdot V = l_t + l_x\tilde{u} + l_y\tilde{v} + l_z\tilde{w} \tag{7}$$

$$V = m_t + m \cdot V = m_t + m_x\tilde{u} + m_y\tilde{v} + m_z\tilde{w} \tag{8}$$

$$W = n_t + n \cdot V = n_t + n_x\tilde{u} + n_y\tilde{v} + n_z\tilde{w} \tag{9}$$

where J is the Jacobian of the coordinate transformation. l_t, m_t and n_t are the components of the interface contravariant velocity of the grid in ξ, η and ζ directions respectively. l, m and n denote the normal vectors located at the centers of ξ, η and ζ interfaces of the control volume with their magnitudes equal to the surface areas and pointing to the directions of increasing ξ, η and ζ.

$$l = \frac{\nabla\xi}{J}, \qquad m = \frac{\nabla\eta}{J}, \qquad n = \frac{\nabla\zeta}{J} \tag{10}$$

$$l_t = \frac{\xi_t}{J}, \qquad m_t = \frac{\eta_t}{J}, \qquad n_t = \frac{\zeta_t}{J} \tag{11}$$

In the generalized coordinates, $\Delta\xi = \Delta\eta = \Delta\zeta = 1$. Since the DES-family approach is based on S-A model, the formulations of the original S-A model are give below. The source term S_ν from the S-A model in Eq. 7, is given by

$$S_\nu = \bar{\rho} C_{b1}(1 - f_{t2})\tilde{S}\tilde{\nu} + \frac{1}{Re}\left[-\bar{\rho}\left(C_{w1} f_w - \frac{C_{b1}}{\kappa^2} f_{t2}\right)\left(\frac{\tilde{\nu}}{d}\right)^2\right. \tag{12}$$

$$\left. + \frac{\bar{\rho}}{\sigma} C_{b2}(\nabla\tilde{\nu})^2 - \frac{1}{\sigma}(\nu + \tilde{\nu})\nabla\tilde{\nu}\cdot\nabla\bar{\rho}\right] + Re\left[\bar{\rho} f_{t1}(\Delta q)^2\right] \tag{13}$$

where

$$\chi = \frac{\tilde{\nu}}{\nu}, \qquad f_{v1} = \frac{\chi^3}{\chi^3 + c_{v1}^3}, \qquad f_{v2} = 1 - \frac{\chi}{1 + \chi f_{v1}} \tag{14}$$

$$f_{t1} = C_{t1} g_t \exp\left(-C_{t2}\frac{\omega_t^2 \Delta U^2}{d^2 + g_t^2 d_t^2}\right) \tag{15}$$

$$f_{t2} = C_{t3}\exp(-C_{t4}\chi^2), \qquad f_w = g\left(\frac{1 + c_{w3}^6}{g^6 + c_{w3}^6}\right)^{1/6}, \qquad g = r + c_{w2}(r^6 - r) \tag{16}$$

$$g_t = \min\left(0.1, \frac{\Delta q}{\omega_t \Delta x_t}\right), \qquad \tilde{S} = S + \frac{\tilde{\nu}}{\kappa^2 d^2 Re} f_{v2}, \qquad r = \frac{\tilde{\nu}}{\tilde{S}\kappa^2 d^2 Re} \tag{17}$$

where, ω_t is the wall vorticity at the wall boundary layer trip location, d is the distance to the closest wall, d_t is the distance of the field point to the trip location, Δq is the difference of the velocities between the field point and the trip location, Δx_t is the grid spacing along the wall at the trip location. The values of the coefficients are: $c_{b1} = 0.1355$, $c_{b2} = 0.622$, $\sigma = \frac{2}{3}$, $c_{w1} = \frac{c_{b1}}{\kappa^2} + \frac{1 + c_{b2}}{\sigma}$, $c_{w2} = 0.3$, $c_{w3} = 2$, $\kappa = 0.41$, $c_{v1} = 7.1$, $c_{t1} = 1.0$, $c_{t2} = 2.0$, $c_{t3} = 1.1$, $c_{t4} = 2.0$.

The shear stress $\bar{\tau}_{ik}$ and total heat flux $\bar{q}_k$ in Cartesian coordinates is given by

$$\bar{\tau}_{ik} = (\mu + \mu_{IDDES})\left(\frac{\partial\tilde{u}_i}{\partial x_k} + \frac{\partial\tilde{u}_k}{\partial x_i} - \frac{2}{3}\delta_{ik}\frac{\partial\tilde{u}_j}{\partial x_j}\right) \tag{18}$$

$$\bar{q}_k = -\left(\frac{\mu}{Pr} + \frac{\mu_{IDDES}}{Pr_t}\right)\frac{\partial\tilde{T}}{\partial x_k} \tag{19}$$

where μ is from Sutherland's law. For IDDES approach in general, the eddy viscosity is represented by μ_{IDDES} $(= \bar{\rho}\tilde{\nu} f_{v1})$.

2.2 Improved Delayed Detached Eddy Simulation (IDDES)

The Improved DDES (IDDES) is introduced by extending the DDES with the WMLES capacity. The IDDES has two branches, DDES and WMLES, including a set of empirical functions of subgrid length-scales designed to achieve good performance from these branches themselves and their coupling. By switching the activation of RANS and LES in different flow regions, IDDES significantly expands the scope of application of DDES with well-balanced and powerful numerical approach to complex turbulent flows at high Reynolds numbers.

2.2.1 DDES branch of IDDES

The DDES branch is responsible for the DDES-like functionality of IDDES and should become active only when the inflow conditions do not have any turbulent content (if a simulation has spatial periodicity, the initial conditions rather than the inflow conditions set the characteristics of the simulation), in particular when a grid of "boundary-layer type" precludes the resolution of the dominant eddies. The DDES formulation can be reformulated as

$$l_{DDES} = l_{RANS} - f_d \max\{0, l_{RANS} - l_{LES}\} \tag{20}$$

where the delaying function, f_d, is defined the same as

$$f_d = 1 - \tanh[(8r_d)^3] \tag{21}$$

and the quantity r_d borrowed from the S-A RANS turbulence model:

$$r_d = \frac{\nu_t + \nu}{\kappa^2 d_w^2 \max[(U_{i,j}U_{i,j})^{0.5}, 10^{-10}]} \tag{22}$$

is a marker of the wall region, which is equal to 1 in a log layer and 0 in a free shear flow.

In Eq. 23, $U_{i,j}$ represents the velocity gradient, and κ denotes the Karmann constant. Based on the general DES concept, in order to create a seamless hybrid model, the length-scale IDDES defined by Eq.15 is substituted into the background RANS model to replace the RANS length-scale, l_{RANS}, which is explicitly or implicitly involved in any such model. For instance, for the S-A model the length-scale is equal to the distance to the wall $l_{RANS} = d_w$. In the original DES97, the length-scale depends only on the local grid. In DDES and IDDES, it also depends on the solution of Eq. 21 and 23.

The LES length-scale, l_{LES}, is defined via the subgrid length-scale for Eq. 15 as

$$l_{LES} = C_{DES}\Phi\Delta \tag{23}$$

where C_{DES} is the fundamental empirical constant of DES, 0.65. Φ is a low-Reynolds number correction introduced in order to compensate the activation of the low-Reynolds number terms of some background RANS model in LES mode. Both C_{DES} and Φ depend on the background RANS model, and Ψ is equal to 1 if the RANS model does not include any low-Reynolds number terms.

2.2.2 WMLES branch of IDDES

The WMLES branch is intended to be active only when the inflow conditions used in the simulation are unsteady and impose some turbulent content with the grid fine enough to resolve boundary-layer dominant eddies. It presents a new seamless hybrid RANS-LES model, which couples RANS and LES approaches via the introduction of the following blended RANS-LES length-scale:

$$l_{WMLES} = f_B(1 + f_e)l_{RANS} + (1 - f_B)l_{LES} \tag{24}$$

The empirical blending-function f_B depends upon d_w/h_{max} and is defined as

$$f_B = \min\{2\exp(-9\alpha^2), 1.0\}, \quad \alpha = 0.25 - d_w/h_{max} \tag{25}$$

It varies from 0 to 1 and provides rapid switching of the model from RANS mode ($f_B = 1.0$) to LES mode ($f_B = 0$) within the range of wall distance $0.5h_{max} < d_w < h_{max}$

The second empirical function involved in Eq. 19, elevating-function, f_e, is aimed at preventing the excessive reduction of the RANS Reynolds stresses observed in the interaction of the RANS and LES regions in the vicinity of their interface. It is intended to eliminating the log-layer mismatch (LLM) problem.

$$f_e = \max\{(f_{e1} - 1), 0\}\Phi f_{e2} \tag{26}$$

where the function f_{e1} is defined as

$$f_{e1}(d_w/h_{max}) = \begin{cases} 2\exp(-11.09\alpha^2) & \text{if } \alpha \geq 0 \\ 2\exp(-9.0\alpha^2) & \text{if } \alpha < 0 \end{cases} \tag{27}$$

It provides a grid-dependent "elevating" device for the RANS component of the WMLES length-scale.

The function f_{e2} is:

$$f_{e2} = 1.0 - \max\{f_t, f_l\} \tag{28}$$

2.2.3 Blending DDES and WMLES branches

The DDES length-scale defined by Eq. 21 and that of the WMLES-branch defined by Eq. 25 do not blend directly in a way to ensure an automatic choice of the WMLES or DDES mode by the combined model, depending on the type of the simulation (with or without turbulent content) and the grid used.

However a modified version of equivalent length scale combination, namely,

$$\tilde{l}_{DDES} = \tilde{f}_d l_{RANS} + (1 - \tilde{f}_d) l_{LES} \tag{29}$$

where the blending function $\tilde{f}_d$ is defined by

$$\tilde{f}_d = \max\{(1 - f_{dt}), f_B\} \tag{30}$$

with $f_{dt} = 1 - \tanh[(8r_{dt})^3]$

With the use of Eq. 29, the required IDDES length-scale combining the DDES and WMLES length scales defined by Eqns. 30 and 25 is straightforward and can be implemented as

$$l_{hyb} = \tilde{f}_d(1 + f_e) l_{RANS} + (1 - \tilde{f}_d) l_{LES} \tag{31}$$

With inflow turbulent content, f_{dt} is close to 1.0, $\tilde{f}_d$ is equal to f_B, so Eq. 31 is reduced to $l_{hyb} = l_{WMLES}$ in Eq. 25. Otherwise, f_e is zero, Eq. 31 is interpreted as $l_{hyb} = l_{DDES}$ in Eq. 30.

2.3 Time Marching Scheme

Following the dual time stepping method suggested by Jameson [37], an implicit pseudo time marching scheme using line Gauss-Seidel line relaxation is employed to solve the governing equations, as the

following:

$$\frac{\partial Q}{\partial t} = \frac{3Q^{n+1} - 4Q^n + Q^{n-1}}{2\Delta t} \tag{32}$$

where $n-1$, n and $n+1$ are three sequential time levels, which have a time interval of Δt. The first-order Euler scheme is used to discretize the pseudo temporal term. The semi-discretized equations of the governing equations are given as the following:

$$\left[\left(\frac{1}{\Delta\tau} + \frac{1.5}{\Delta t}\right) I - \left(\frac{\partial R}{\partial Q}\right)^{n+1,m}\right] \delta Q^{n+1,m+1} = R^{n+1,m} - \frac{3Q^{n+1,m} - 4Q^n + Q^{n-1}}{2\Delta t} \tag{33}$$

where the $\Delta\tau$ is the pseudo time step, and R stands for the net flux determined by the spatial high order numerical scheme, m is the iteration index for the pseudo time.

2.4 Lift and Drag Calculation

The momentum and pressure at the injection and suction slots produce a reactionary force, which must included in CFD simulation. Using control volume analysis, the reactionary force can be calculated using the flow parameters at the injection and suction slot opening surfaces. Zha et al. [6] give the following formulations to calculate the lift and drag due to the jet reactionary force for a CFJ airfoil. By considering the effects of injection and suction jets on the CFJ airfoil, the expressions for these reactionary forces are given as :

$$F_{x_{cfj}} = (\dot{m}_j V_{j1} + p_{j1} A_{j1}) * cos(\theta_1 - \alpha) - (\dot{m}_j V_{j2} + p_{j2} A_{j2}) * cos(\theta_2 + \alpha) \tag{34}$$

$$F_{y_{cfj}} = (\dot{m}_{j1} V_{j1} + p_{j1} A_{j1}) * sin(\theta_1 - \alpha) + (\dot{m}_{j2} V_{j2} + p_{j2} A_{j2}) * sin(\theta_2 + \alpha) \tag{35}$$

where the subscripts 1 and 2 stand for the injection and suction respectively, and θ_1 and θ_2 are the angles between the injection and suction slot's surface and a line normal to the airfoil chord[6]. α is the angle of attack.

The total lift and drag on the airfoil can then be expressed as:

$$D = R'_x - F_{x_{cfj}} \tag{36}$$

$$L = R'_y - F_{y_{cfj}} \tag{37}$$

where R'_x and R'_y are the surface integral of pressure and shear stress in x (drag) and y (lift) direction excluding the internal ducts of injection and suction. For CFJ airfoil simulations, the total lift and drag are calculated by integrating Eqs.(36) and (37) in the spanwise direction.

2.5 Jet Momentum Coefficient

The jet momentum coefficient C_μ is a parameter used to quantify the jet intensity. It is defined as:

$$C_\mu = \frac{\dot{m} V_j}{\frac{1}{2}\rho_\infty {V_\infty}^2 S} \tag{38}$$

where $\dot{m}$ is the injection mass flow, V_j is the mass-averaged injection velocity, ρ_∞ and V_∞ denote the free stream density and velocity, and S is the planform area.

2.6 Micro-compressor Power Coefficient

CFJ is implemented by mounting a pumping system inside the airfoil that withdraws air from the suction slot and blows it into the injection slot. The power consumption is determined by the jet mass flow and total enthalpy change as the following:

$$P = \dot{m}(H_{t1} - H_{t2}) \tag{39}$$

where H_{t1} and H_{t2} are the mass-averaged total enthalpy in the injection cavity and suction cavity respectively, P is the Power required by the pump and $\dot{m}$ the jet mass flow rate. Introducing P_{t1} and P_{t2} as the mass-averaged total pressure in the injection and suction cavity respectively, the compressor efficiency η, and the total pressure ratio of the pump $\Gamma = \frac{P_{t1}}{P_{t2}}$, the power consumption is expressed as:

$$P = \frac{\dot{m} C_p T_{t2}}{\eta}(\Gamma^{\frac{\gamma-1}{\gamma}} - 1) \tag{40}$$

where γ is the specific heat ratio equal to 1.3 for Martian air , C_p is the specific heat at constant pressure, T_t is the total pressure at the suction slot, η is the CFJ micro-compressor actuator efficiency. The power coefficient is expressed as:

$$P_c = \frac{P}{\frac{1}{2}\rho_\infty V_\infty^3 S} \tag{41}$$

2.7 Aerodynamic Efficiency

The conventional airfoil aerodynamic efficiency is defined as:

$$\frac{C_L}{C_D} \tag{42}$$

For the CFJ airfoil, the ratio above still represents the pure aerodynamic relationship between lift coefficient and drag coefficient. However since CFJ active flow control consumes energy, the ratio above is modified to take into account the energy consumption of the micro-compressor. The formulation of the corrected aerodynamic efficiency for CFJ airfoils is given in Eqn.1. If the micro-compressor power coefficient is set to 0, Eqn.1 returns to the aerodynamic efficiency of a conventional airfoil.

2.8 CFD Simulation Setup

The in house FASIP(Flow-Acoustics-Structure Interaction Package) CFD code is used to conduct the numerical simulation. The 3D Unsteady Navier-Stokes equations with IDDES turbulence model is used. A 5th order WENO scheme for the inviscid flux [38–43] and a 2nd order central differencing for the viscous terms [38, 42] are employed to discretize the Navier-Stokes equations. The low diffusion E-CUSP scheme used as the approximate Riemann solver suggested by Zha et al [39] is utilized with the WENO scheme to evaluate the inviscid fluxes. Implicit time marching method using Gauss-Seidel line relaxation is used to achieve a fast convergence rate [44]. Parallel computing is implemented to save wall clock simulation time [45].

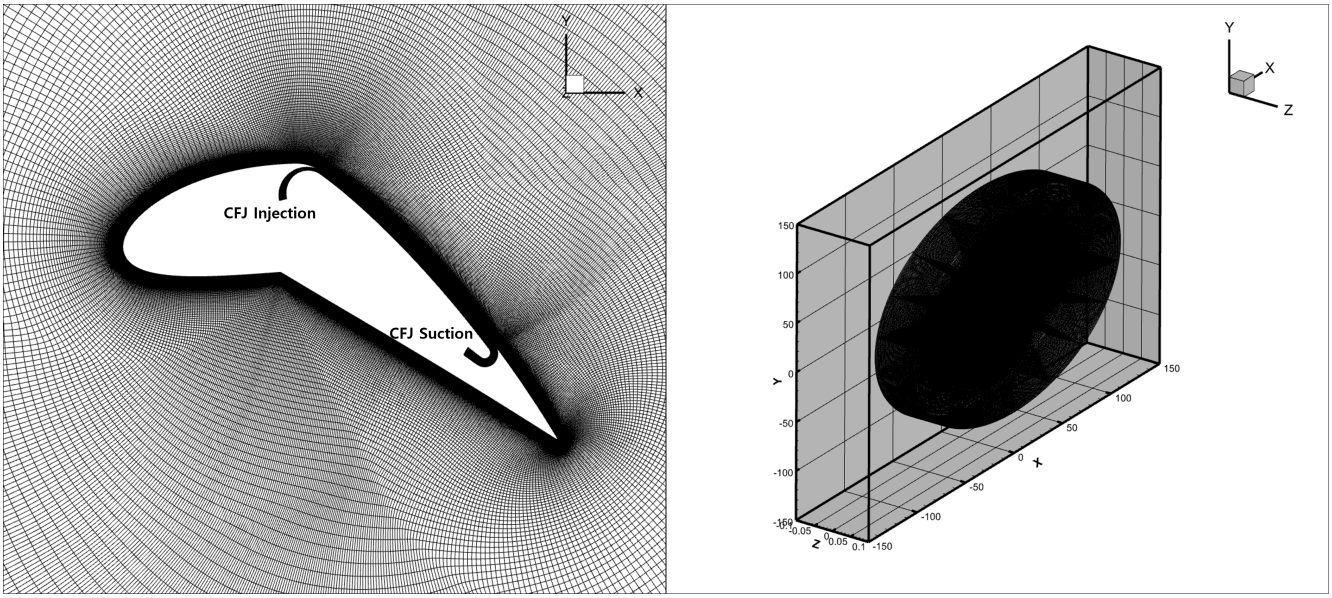

Figure 2: Computational mesh used in the current work.

Table 1: Flow Conditions and Properties

Variable	**Value**	**Unit**
p	655	[Pa]
T	220	[K]
ρ	0.01575	[kg/m^3]
μ	1.11E-05	[kg/m s]
R	188.9	[J/kg K]
L_{ref}	1	[m]
U_∞	39.53	[m/s]
γ	1.3	
M_∞	0.17	
Re_∞	5.63E+04	

2.9 Boundary Conditions

The 3rd order accuracy no slip condition is enforced on the solid surface with the wall treatment suggested in [46] to achieve the flux conservation on the wall. The far field boundary is located at 100 chord with a O-mesh topology. The computational mesh is shown in Fig. 2. The simulated span is 10% of the chord length, with periodic boundary conditions applied in the spanwise direction to obtain sectional performance characteristics. Total pressure, total temperature and flow angles are specified at the upstream portion of the far field. Constant static pressure is applied at the downstream portion of the far field. The first grid point on the airfoil surface is placed at $y^+ \approx 1$. The computational mesh consists of $540 \times 240 \times 40$ grid points in the streamwise, normal, and spanwise directions, respectively, resulting in approximately 5.2 million cells.

The atmospheric properties for Mars, relevant to the present analysis, are summarized in Table 1.

3 Results and Discussion

Flow analysis is performed at M=0.17, Re=56,300 with a jet momentum coefficient C_μ=0.25 . The results from 2D RANS using the SA turbulence model and 3D IDDES show very similar characteristics, as demonstrated in Figs. 3 and 4. The C_p distributions shown in Fig. 5 are nearly identical, although the 3D IDDES case exhibits a slightly lower C_L value. This discrepancy is further investigated through mesh refinement studies and the use of higher-order schemes. Fig. 6 shows the isosurface with the Q criterion = 1, where the turbulent structures are not clearly resolved due to insufficient mesh density, indicating that studies with higher mesh resolution are necessary.

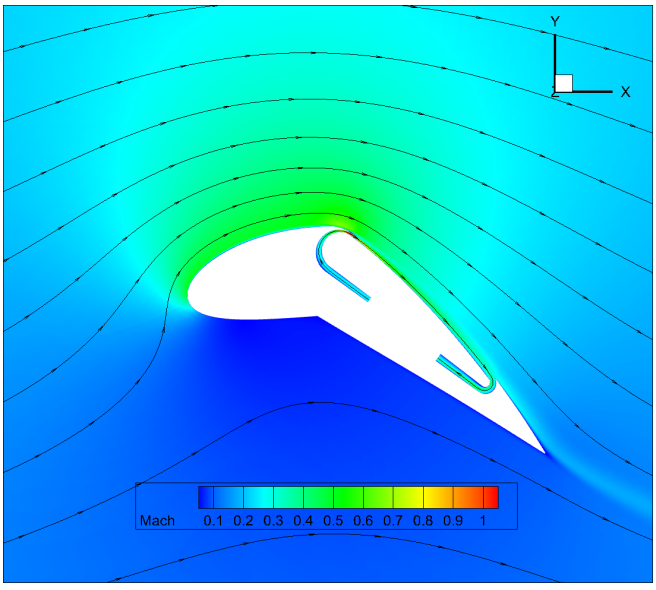

Figure 3: Mach contour of 2D RANS

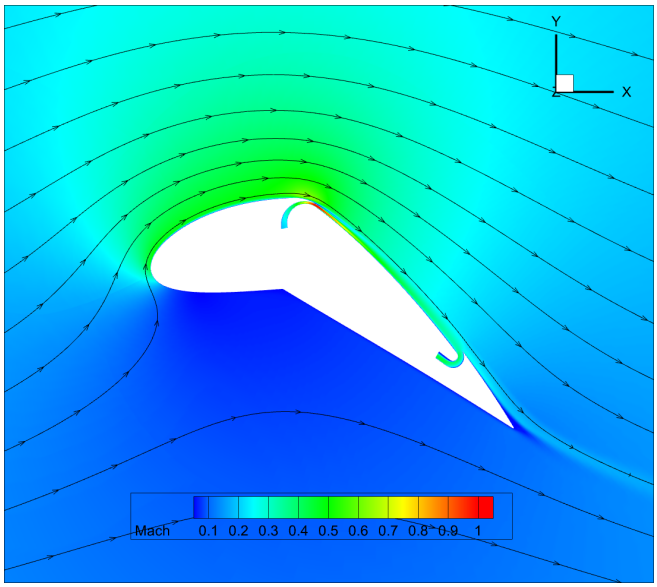

Figure 4: Mach contour of 3D IDDES

Table 2: Comparison of aerodynamic performance between 2D RANS and 3D IDDES

Case	C_L	C_D	C_L/C_D	$P_{t,ratio}$	P_c	$C_L/(C_D+P_c)$	$C_L^2/(C_D+P_c)$
2D RANS	4.87	0.003	1493.00	1.464	0.538	8.99	43.74
3D IDDES	4.63	0.009	521.97	1.485	0.568	8.02	37.10

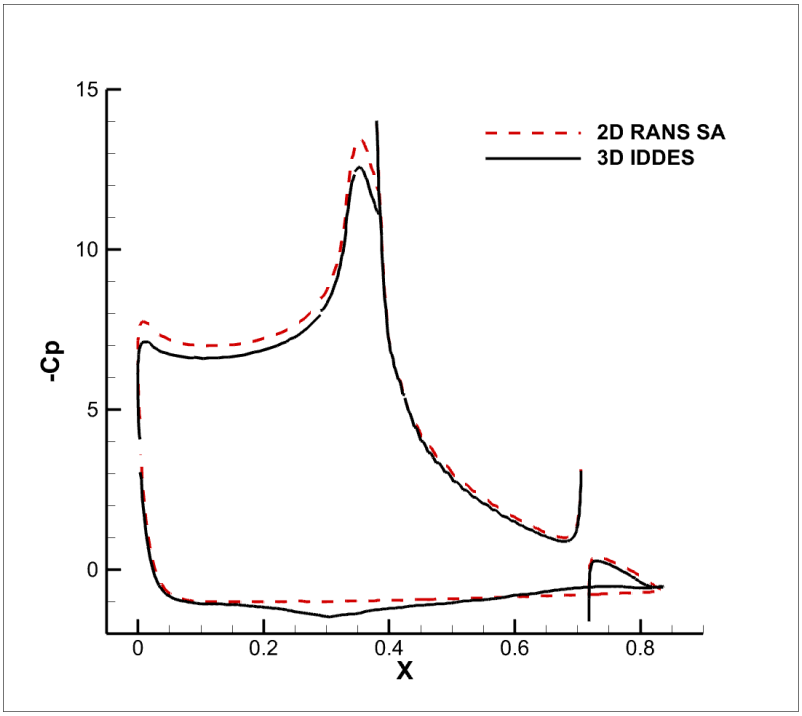

Figure 5: C_p distribution

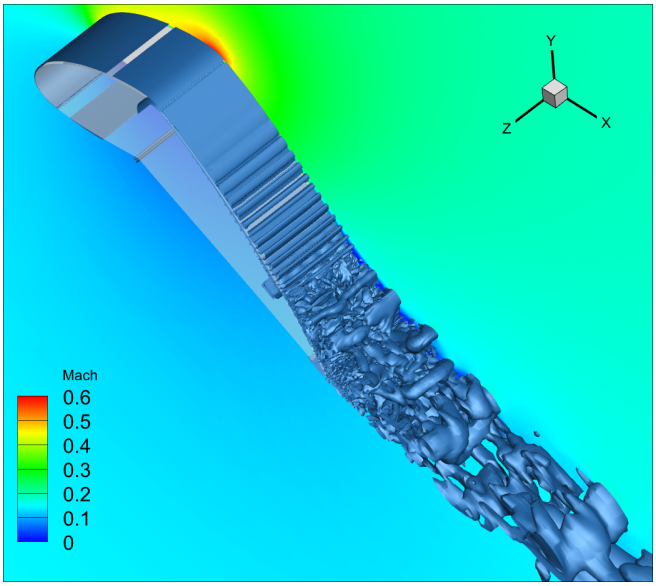

Figure 6: Isosurface with the Q criterion = 1

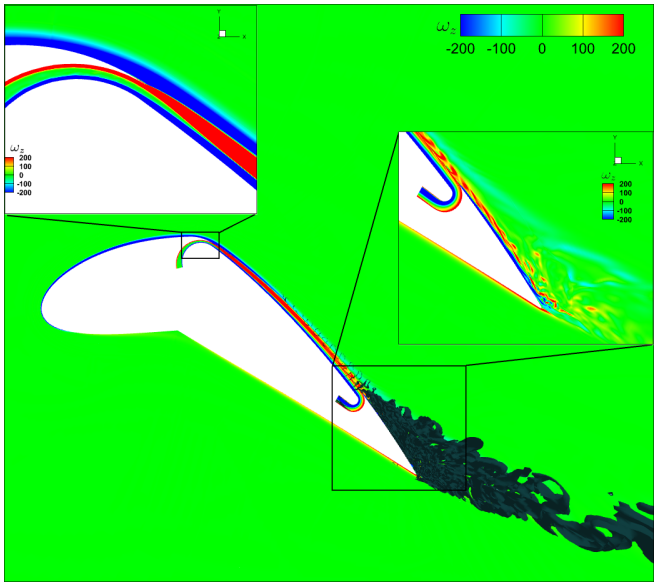

Figure 7: Vorticity distribution

3.1 Mechanism of Flow Attachment

The turbulent wall jet momentum equation is employed to evaluate the flow attachment characteristics on the surface. This methodology has been previously utilized to analyze the flow for the 2D NASA hump [25]. The approach is adopted here to enhance our understanding of the APG flow at low Reynolds number simulated by 3D IDDES. The wall jet momentum equation is applied in its 2D form, assuming plane flows in the evaluated regions, while acknowledging this represents an approximation for flows with low curvature geometry. Although analysis with high curvature in [47] demonstrates that the dominant terms of the wall jet equation remain consistent, this approach is used to estimate the contribution of each term to maintaining flow attachment.

In the following equations, x denotes the local streamwise direction tangent to the wall surface, and y represents the direction normal to the wall surface. The viscosity μ comprises both molecular viscosity and turbulent eddy viscosity. The turbulent wall jet momentum equation in the x direction can be expressed in non-dimensional, partial difference form as follows [48]:

$$\rho u\frac{\partial u}{\partial x}+\rho v\frac{\partial u}{\partial y}-\frac{1}{Re}\frac{\partial \mu}{\partial y}\frac{\partial u}{\partial y}+\frac{\partial p}{\partial x}=\frac{1}{Re}\mu\frac{\partial^2 u}{\partial y^2} \tag{43}$$

A more comprehensive criterion for separation control has been proposed by Xu et al. [25, 48]. This separation criterion applies to both laminar and turbulent flows. They suggest that it is more energy efficient to achieve "attached elevated flows" with adverse pressure gradients rather than attached flows with favorable pressure gradients. The attached velocity profiles satisfy $\tau_w > 0$ (i.e., $\partial u/\partial y > 0$, $\omega_z < 0$) with $[\partial^2 u/\partial y^2]_w \geq 0$. The condition $[\partial^2 u/\partial y^2]_w = 0$ corresponds to zero pressure gradient situations. Flow separation occurs when $\partial u/\partial y < 0$ [48].

An adverse pressure gradient can be overcome along a wall through the flow's momentum convection and turbulence diffusion. The first two terms on the left-hand side of Eq. (43) represent the convective terms the inertia force term and spanwise vorticity flux, which are responsible for transferring wall jet momentum in the streamwise and transverse flow directions. In wall jet flows, these two terms exhibit similar magnitudes due to the high velocity gradient imposed by CFJ injection [48]. The third term represents momentum diffusion due to the turbulent eddy viscosity gradient. While this term is negligible for laminar flow due to relatively constant viscosity, it becomes dominant for turbulent mixing owing to the significant growth rate of turbulent eddy viscosity near the wall in CFJ applications [25, 47]. This turbulent diffusion is particularly important for maintaining attached flow under APG conditions. All three terms on the left-hand side of Eq. (43) contribute to offsetting the adverse pressure gradient; however, the diffusion term plays the most significant role in transferring momentum inward to energize the turbulent boundary layer and outward to entrain the main flow.

The velocity gradient at the wall can be expressed in terms of spanwise vorticity through the substitution:

$$\omega_z=\frac{\partial v}{\partial x}-\frac{\partial u}{\partial y}\approx-\frac{\partial u}{\partial y} \tag{44}$$

For an injection wall jet tangential to the wall surface, $\frac{\partial v}{\partial x} \ll \frac{\partial u}{\partial y}$ except in the region near the suction slot entrance. The wall jet momentum equation (43) may then be rewritten as:

$$\rho u\frac{\partial u}{\partial x} - \rho v\omega_z + \frac{\omega_z}{Re}\frac{\partial \mu}{\partial y} + \frac{\partial p}{\partial x} = \frac{\mu}{Re}\frac{\partial^2 u}{\partial y^2} \tag{45}$$

The strong spanwise vorticity flux along the CFJ's injection duct surfaces plays a crucial role in maintaining wall jet flow attachment.

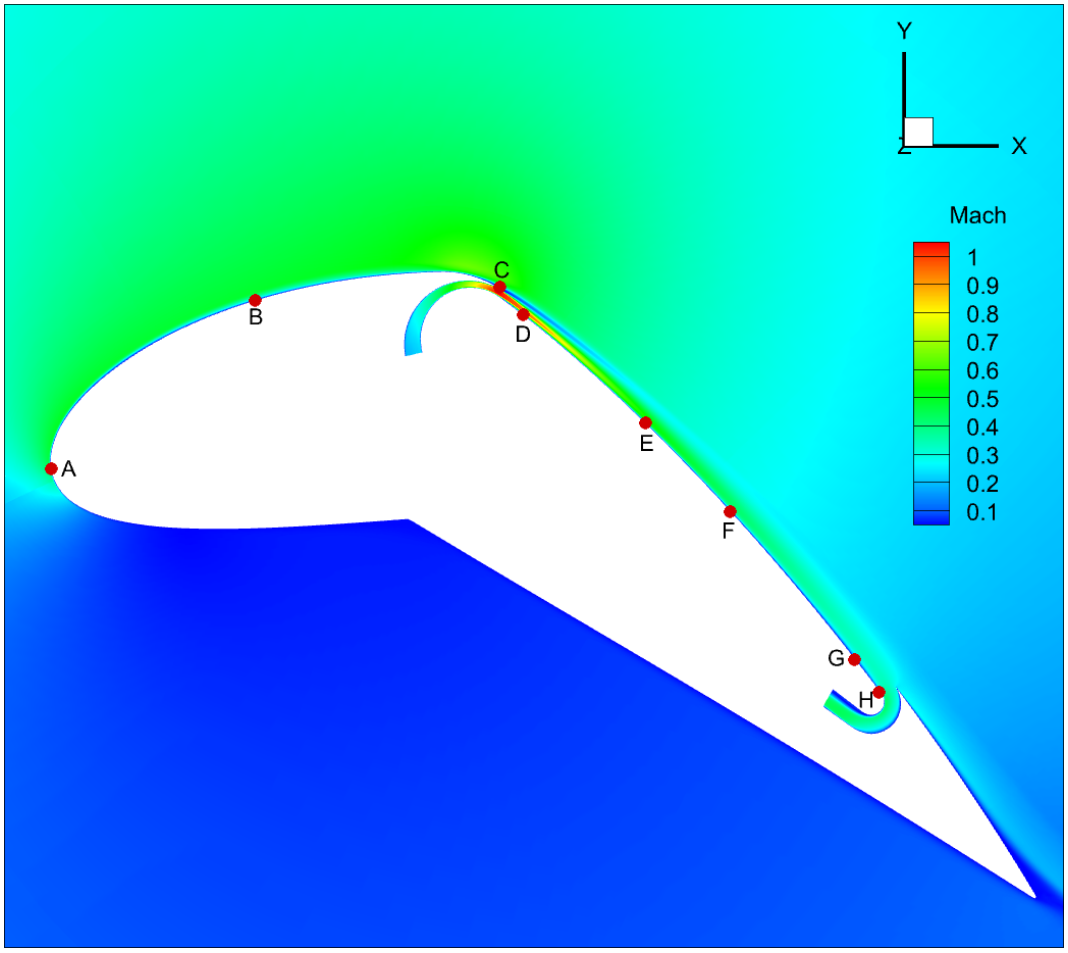

Figure 8: Positions for evaluating flow attachment

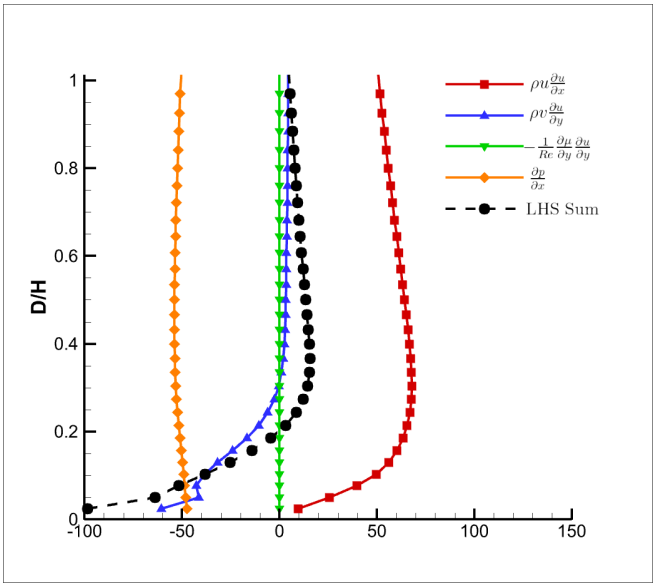

Figure 9: Position A

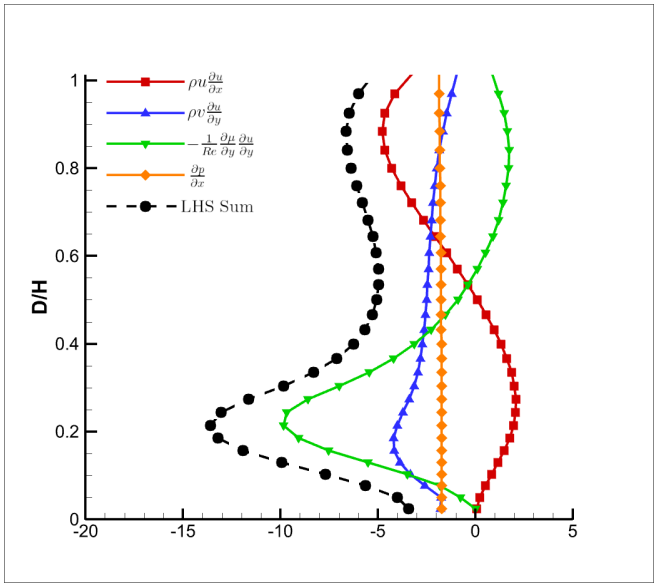

Figure 10: Position B

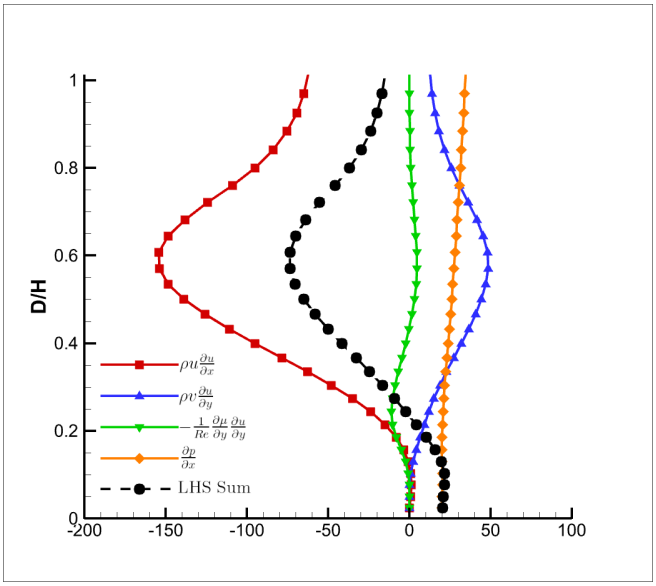

Figure 11: Position C

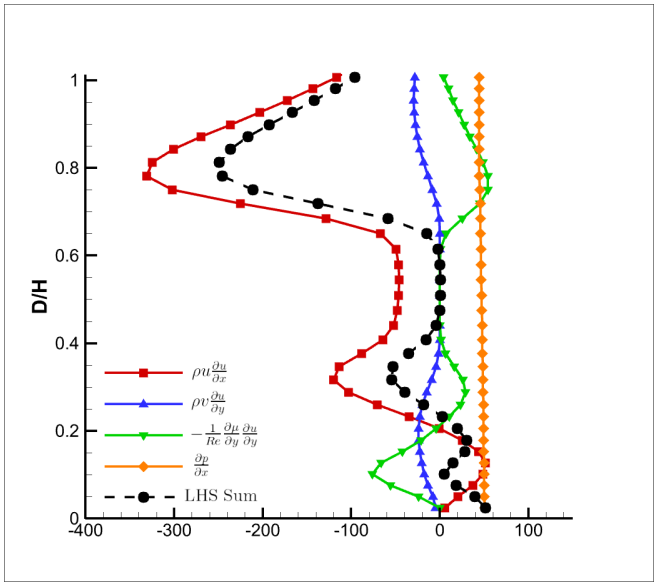

Figure 12: Position D

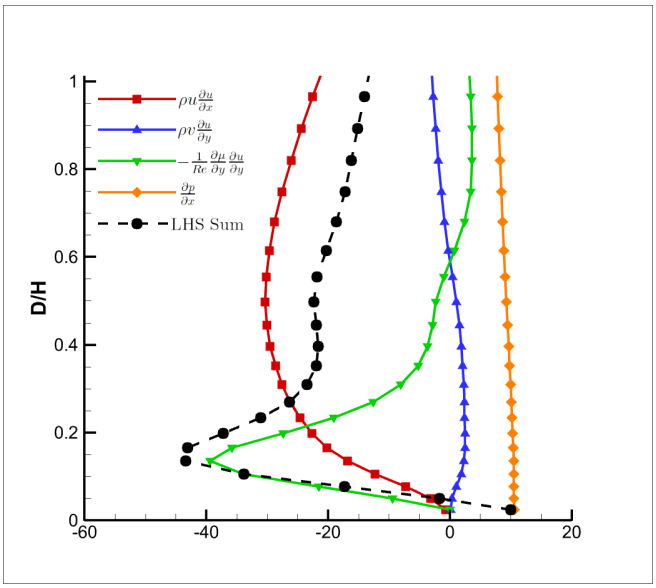

Figure 13: Position E

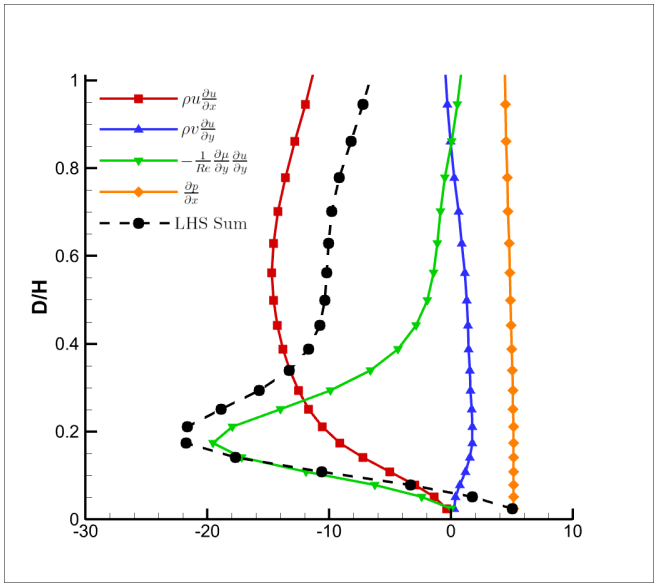

Figure 14: Position F

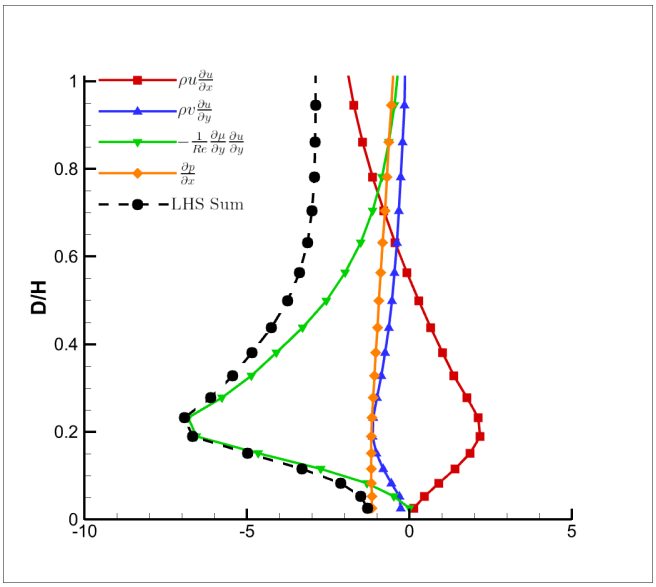

Figure 15: Position G

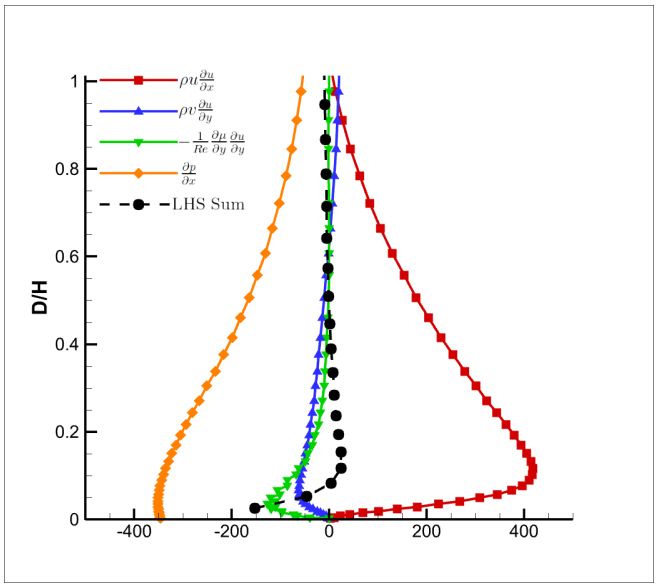

Figure 16: Position H

The detailed flow physics at different locations (Positions A-H in Fig. 8) are analyzed below based on the wall jet momentum equation.

Position A is located near the leading edge stagnation point. In this region, the flow accelerates rapidly around the nose, creating a strong favorable pressure gradient. This dp/dx term acts as the primary driving force, pushing the flow downstream and keeping it attached. The spanwise vorticity flux term $\rho v \partial u/\partial y$ is also identified as important for flow attachment, mostly due to the converging streamline that induces the transverse velocity component v pointing toward the wall. (Fig. 9).

Position B is situated between the leading edge and the start of the flap. Moving downstream, the flow

remains in a favorable pressure gradient region, but the acceleration slows down, reducing the magnitude of dp/dx compared to the leading edge (Fig. 10). As the boundary layer develops, the turbulent eddy viscosity diffusion term begins to play a more substantial role. This indicates that turbulent transport of momentum towards the wall is becoming necessary to supplement the pressure gradient in maintaining flow attachment.

Position C is located on the airfoil surface immediately upstream of the CFJ injection. Here, the streamwise inertia momentum is the dominant factor (Fig. 11). This term represents the convection of momentum within the boundary layer before it interacts with the high-speed jet, serving as the inertial force crucial for carrying the flow over the slot geometry.

Position D represents the flow immediately downstream of the CFJ injection slot, where the high-velocity jet enters the flow field and mixes with the external flow. The flow phenomena in this region appear highly complex due to the intense shear layer interaction. For flow attachment, the streamwise inertia momentum exhibits a very large value (Fig. 12), reflecting the massive injection of momentum from the jet which serves as the primary energy source for the flow control.

In the regions E and F, over the flap surface where the CoFlow Jet is fully established, the flow is well attached. Here, the turbulent eddy viscosity diffusion term is a major contributor (Figs. 13 and 14). This term representsa strong mixing between the high energy jet and the main flow, which energize the boundary layer. The streamwise inertia momentum also makes a strong contribution due to the jet momentum and the adverse pressure gradient that generates a negative acceleration $\partial u/\partial x$, which in turn offsets the adverse pressure itself.

As the flow approaches the suction slot at Position G, a local favorable pressure gradient is created by the suction, which helps to attach the flow. At the same time, the injection jet decays due to mixing and wall friction. Consequently, while the turbulent diffusion term remains the most dominant factor in maintaining attachment due to the suction, its magnitude is significantly reduced compared with the upstream points such as E and F, the upstream flap region(Fig. 15).

At Position H, immediately upstream of the suction slot, the flow enters the low pressure region created by the micro-compressor actuator. The low pressure of the suction creates a very strong localized favorable pressure gradient. Consequently, dp/dx is observed to have the greatest influence on flow attachment (Fig. 16), effectively guiding the boundary layer into the slot.

In this study, the Reynolds number is 56,300, which is a laminar regime where separation can occur easily. In the favorable pressure gradient regions (Positions A-C), the flow can remain attached. However, in the adverse pressure gradient regions (Positions D-H), the flow can easily be separated without flow control. Although the jet supplied by the CoFlow Jet may be laminar at the injection exit with a Reynolds number of 1590, mixing with the external flow triggers laminar-turbulence transition and increases the turbulent intensity. As shown in Fig. 7, the vorticity magnitude increases significantly after the injection. This enhanced vorticity promotes mixing and momentum transfer, making the turbulent eddy diffusion term dominant in attaching the flow in the adverse pressure gradient regions (Positions D-H).

4 Conclusion

This paper investigates the flow physics of a flapped coflow jet (FCFJ) airfoil using IDDES at the low Reynolds number conditions of the Martian atmosphere. The results demonstrate that the FCFJ

airfoil can achieve ultra-high lift coefficients and high aerodynamic efficiency under Martian atmospheric conditions. A detailed analysis using the turbulent wall jet momentum equation reveals the mechanism of flow attachment at different locations on the airfoil. Near the leading edge (Positions A and B), the favorable pressure gradient and spanwise vorticy flux at the wall convection are dominant. In the injection region (Positions C and D), the streamwise inertia force term plays a critical role. As the flow develops over the flap (Positions E and F), turbulent diffusion becomes the primary mechanism for maintaining flow attachment, supported by streamwise inertia force term. Approaching the suction slot (Positions G and H) the local favorable pressure gradient is the dominant contribution to attach the flow, whereas the turbulent diffusion remain an important factor.

These findings provide fundamental insights into how coflow jet active flow control achieves attached flow at low Reynolds numbers, paving the way for the development of efficient aerial vehicles for future Mars exploration missions. Future work will employ Large Eddy Simulation (LES) to further investigate these flow phenomena with greater fidelity.

5 Acknowledgment

The authors would like to acknowledge the computing resources provided by CoFlow Jet,LLC. The teaching assistantship support from the University of Miami is also acknowledged.

Disclosure: The University of Miami and Dr. Gecheng Zha may receive royalties for future commercialization of the intellectual property used in this study. The University of Miami is also equity owner in CoFlow Jet, LLC, licensee of the intellectual property used in this study.

References

[1] Koji FUJITA, Remi LUONG, Hiroki NAGAI, and Keisuke ASAI. Conceptual Design of Mars Airplane. *Trans. JSASS Aerospace Tech. Japan, Vol.10, No.ists28, pp.5-10*, 2012. doi: 10.2322/tastj.10.te_5.

[2] Gecheng Zha, Yan Ren, Miranda Anhalzer, Michael A. Mischna, and Michael M. Sori. Mars Aerial and Ground Global Intelligent Explorer (MAGGIE): Mission Feasibility Study. *Proceedings of AIAA SciTech Forum*, 2026.

[3] Gecheng Zha, Yan Ren, and William Fredericks. Design and Testing of Deflected Slipstream Airfoil for VTOL Hover Enabled by CoFlow Jet. *AIAA Paper 2024-4420 , AIAA AVIATION FORUM AND ASCEND 2024, 29 July - 2 August 2024, Las Vegas, Nevada*, 2024. doi: 10.2514/6.2024-4420.

[4] Yan Ren Jaehyoung Jeon and Gecheng Zha. Toward Ultra-High Cruise Lift Coefficient Using Flapped CoFlow Jet Airfoil. *AIAA 2023-1008, AIAA SciTech Forum*, 2023. doi: 10.2514/6.2023-1008.

[5] G.-C. Zha and D. C. Paxton. A Novel Flow Control Method for Airfoil Performance Enhancement Using Co-Flow Jet. *Applications of Circulation Control Technologies*, Chapter 10, p. 293-314, Vol. 214, Progress in Astronautics and Aeronautics, AIAA Book Series, Editors: Joslin, R. D. and Jones, G.S., 2006.

[6] G.-C. Zha, W. Gao, and C. Paxton. Jet Effects on Co-Flow Jet Airfoil Performance. *AIAA Journal*, 45(6):1222–1231, 2007. doi: 10.2514/1.23995.

[7] G.-C Zha, C. Paxton, A. Conley, A. Wells, and B. Carroll. Effect of Injection Slot Size on High Performance Co-Flow Jet Airfoil. *AIAA Journal of Aircraft*, 43, 2006. doi: 10.2514/1.16999.

[8] G.-C Zha, B. Carroll, C. Paxton, A. Conley, and A. Wells. High Performance Airfoil with Co-Flow Jet Flow Control. *AIAA Journal*, 45, 2007. doi: 10.2514/1.20926.

[9] B.-Y. Wang, B. Haddoukessouni, J. Levy, and G.-C. Zha. Numerical Investigations of Injection Slot Size Effect on the Performance of Co-Flow Jet Airfoil. *Journal of Aircraft*, Vol. 45, No. 6,: pp.2084–2091, 2008. doi: 10.2514/1.34567.

[10] B. P. E. Dano, D. Kirk, and G.-C. Zha. Experimental Investigation of Jet Mixing Mechanism of Co-Flow Jet Airfoil. AIAA 2010-4421, 5th AIAA Flow Control Conference, Chicago, IL, 28 Jun - 1 Jul 2010.

[11] B. P. E. Dano, G.-C. Zha, and M. Castillo. Experimental Study of Co-Flow Jet Airfoil Performance Enhancement Using Micro Discreet Jets. AIAA 2011-0941, 49th AIAA Aerospace Sciences Meeting, Orlando, FL, 4-7 January 2011.

[12] A Lefebvre, B Dano, WB Bartow, MD Fronzo, and GC Zha. Performance and energy expenditure of coflow jet airfoil with variation of mach number. *Journal of Aircraft*, 53(6):1757–1767, 2016. doi: 10.2514/1.C033113.

[13] A. Lefebvre and G-C. Zha. Numerical Simulation of Pitching Airfoil Performance Enhancement Using Co-Flow Jet Flow Control. *AIAA 2013-2517*, 2013. doi: 10.2514/6.2013-2517.

[14] A. Lefebvre and G-C. Zha. Cow-Flow Jet Airfoil Trade Study Part I : Energy Consumption and Aerodynamic Performance. *Proceedings of the AIAA Flow Control Conference*, 2014. doi: 10.2514/6.2014-2682.

[15] A. Lefebvre and G-C. Zha. Cow-Flow Jet Airfoil Trade Study Part II : Moment and Drag. *Proceedings of the AIAA Flow Control Conference*, 2014. doi: 10.2514/6.2014-2683.

[16] Yunchao Yang and Gecheng Zha. Super-Lift Coefficient of Active Flow Control Airfoil: What is the Limit? *AIAA 2017-1693, AIAA SCITECH2017, 55th AIAA Aerospace Science Meeting, Grapevine, Texas, 9-13 January 2017*, 2017. doi: 10.2514/6.2017-1693.

[17] Gecheng Zha, Yunchao Yang, Yan Ren, and Brendan McBreen. Super-Lift and Thrusting Airfoil of Coflow Jet Actuated by Micro-Compressors. *AIAA 2018-3061, AIAA AVIATION Forum 2018, Flow Control Conference, June 25-29*, 2018. doi: 10.2514/6.2018-3061.

[18] A. Lefebvre and G.-C. Zha. Trade Study of 3D Co-Flow Jet Wing for Cruise Performance. AIAA Paper 2016-0570, AIAA SCITECH2016, AIAA Aerospace Science Meeting, San Diego, CA, 4-8 January 2016.

[19] Kewei Xu and Gecheng Zha. High Control Authority 3D Aircraft Control Surfaces Using Co-Flow Jet. *AIAA Journal of Aircraft*, 2020. doi: 10.2514/1.C035727.

[20] Kewei Xu, Yan Ren, and Gecheng Zha. Numerical Analysis of Energy Expenditure for Co-Flow Wall Jet Separation Control. *AIAA Journal*, 60(5), 2022. doi: 10.2514/1.J061015.

[21] Yang Wang and Gecheng Zha. Study of Mach Number Effect for 2D Co-Flow Jet Airfoil at Cruise Conditions. *AIAA 2019-3169, AIAA Aviation 2019 Forum, 17-21 June 2019, Dallas, Texas*, 2019. doi: 10.2514/6.2019-3169.

[22] Yan Ren and Gecheng Zha. Performance Enhancement by Tandem Wings Interaction of CoFlow Jet Aircraft. *AIAA 2021-1823, AIAA SciTech Forum, 11–15; 19–21 January 2021, VIRTUAL EVENT*, 2021. doi: 10.2514/6.2021-1823.

[23] Yunchao Yang Yang Wang and Gecheng Zha. Study of Super-Lift Coefficient of Co-Flow Jet Airfoil and Its Power Consumption. *AIAA 2019-3652, AIAA Aviation 2019 Forum, 17-21 June 2019, Dallas, Texas* , 2019. doi: 10.2514/6.2019-3652.

[24] Yan Ren Jaehyoung Jeon, Brendan McBreen and Gecheng Zha. Study of 3D Flapped CoFlow Jet Wings for Ultra-High Cruise Lift Coefficient. *AIAA 2023-4436, AIAA Aviation Forum*, 2023. doi: 10.2514/6.2023-4436.

[25] Kewei Xu, Yan Ren, and Gecheng Zha. Analysis of separation control mechanism of turbulent coflow wall jet. *Elsevier Journal of Aerospace Science and Technology*, 168(110775), 2026. doi: 10.1016/j.ast.2026.110775.

[26] B. McBreen, K.-W. Xu, and G.-C. Zha. Numerical Study of Extreme Adverse Pressure Gradients Enabled by Co-Flow Jet. *AIAA 2023-1430, AIAA SCITECH 2023 Forum, 23-27 January 2023, National Harbor, MD*, 2023. doi: 10.2514/6.2023-1430.

[27] B. McBreen, Y.-C. Yang, and G.-C. Zha. Improved Delayed Detached Eddy Simulation of Co-Flow Jet Flow Control in Extreme Adverse Pressure Gradients. *AIAA Paper 2024-0063, AIAA SCITECH 2024 Forum, 8-12 January 2024, Orlando, FL*, 2024. doi: 10.2514/6.2024-0063.

[28] P.R. Spalart, S. Deck, M.L. Shur, and K.D. Squires. A new Version of Detached-Eddy Simulation, Resistant to Ambiguous Grid Densities. *Theoritical and Computational Fluid Dynamics*, 20:181–195, 2006. doi: 10.1007/s00162-006-0015-0.

[29] P.R. Spalart, W.-H. Jou, M. Strelets, and S.R. Allmaras. Comments on the Feasibility of LES for Wings, and on a Hybrid RANS/LES Approach. Advances in DNS/LES, 1st AFOSR Int. Conf. on DNS/LES, Greyden Press, Columbus, H., Aug. 4-8, 1997.

[30] B. Y Wang and G.-C. Zha. Detached-Eddy Simulation of a Co-Flow Jet Airfoil at High Angle of Attack. AIAA 2009-4015, accepted for publication in Journal of Aircraft, 2011.

[31] Y.-C. Yang and G.-C. Zha. Simulation of Airfoil Stall Flows Using IDDES with High Order Schemes. *AIAA 2016-3185, AIAA AVIATION 2016, 46th AIAA Fluid Dynamics Conference, Washington, D.C., 13-17 June*, 2016. doi: 10.2514/6.2016-3185.

[32] P. Patel and G.-C. Zha. Improved Delayed Detached Eddy Simulation of Separated Flow. *AIAA 2020-3013, AIAA Aviation 2020 Forum, Virtual Event, June 15 - 19*, 2020. doi: 10.2514/6.2020-3013.

[33] P. Patel and G.-C. Zha. Improved Delayed Detached Eddy Simulation of AGARD Wing Flutter with Fully Coupled Fluid-Structure Interaction. *AIAA 2021-0365, AIAA SciTech Forum, VIRTUAL EVENT, 11-15, 19-21 January*, 2021. doi: 10.2514/6.2021-0365.

[34] H-S. Im and G-C. Zha. Delayed Detached Eddy Simulation of Airfoil Stall Flows Using High Order Schemes. *ASME Journal of Fluids Engineering*, 2017. doi: 10.1115/1.4027813.

[35] Im H.-S. Chen X.-C. Zha G.-C. Gan, J.-Y. and C. L. Pasiliao. Delayed detached Eddy simulation of wing flutter boundary using high order schemes. *Journal of Fluids and Structures, Vol. 71, 2017, pp. 199–216.*, 2017. doi: 10.1016/j.jfluidstructs.2017.03.002.

[36] Y.-C. Yang, M. Fernandez, and G.-C. Zha. Improved Delayed Detached Eddy Simulation of Super-Lift Flow of Co-Flow Jet Airfoil. *AIAA 2018-0314, AIAA SciTech Forum, 2018 AIAA Aerospace Sciences Meeting, Kissimmee, FL, 8-12 January*, 2018. doi: 10.2514/6.2018-0314.

[37] Jameson and A. Time Dependent Calculations Using Multigrid with Applications to Unsteady Flows Past Airfoils and Wings. AIAA Paper 91-1596, 1991.

[38] Y.-Q. Shen and G.-C. Zha. Large Eddy Simulation Using a New Set of Sixth Order Schemes for Compressible Viscous Terms . *Journal of Computational Physics*, 229:8296–8312, 2010. doi: 10.1016/j.jcp.2010.07.017.

[39] Shen Y.Q. Zha, G.C. and B.Y. Wang. An improved low diffusion E-CUSP upwind scheme . *Journal of Computer and Fluids*, 48:214–220, 2011. doi: 10.1016/j.compfluid.2011.03.012.

[40] Y.-Q. Shen and G.-Z. Zha. Generalized finite compact difference scheme for shock/complex flowfield interaction. *Journal of Computational Physics*, 2011. doi: 10.1016/j.jcp.2011.01.039.

[41] Y.-Q. Shen, G.-C. Zha, and B.-Y. Wang. Improvement of Stability and Accuracy of Implicit WENO Scheme. *AIAA Journal*, 47, No. 2:331–344, 2009. doi: 10.2514/1.37697.

[42] Y.-Q. Shen, G.-C. Zha, and X.-Y. Chen. High Order Conservative Differencing for Viscous Terms and the Application to Vortex-Induced Vibration Flows. *Journal of Computational Physics*, 228(2): 8283–8300, 2009. doi: 10.1016/j.jcp.2009.08.004.

[43] Y.-Q. Shen and G.-C. Zha. Improvement of the WENO Scheme Smoothness Estimator. *International Journal for Numerical Methods in Fluids*, 2009. doi: 10.1002/fld.2186.

[44] G.-C. Zha and E. Bilgen. Numerical Study of Three-Dimensional Transonic Flows Using Unfactored Upwind-Relaxation Sweeping Algorithm. *Journal of Computational Physics*, 125:425–433, 1996. doi: 10.1006/jcph.1996.0104.

[45] B.-Y. Wang and G.-C. Zha. A General Sub-Domain Boundary Mapping Procedure For Structured Grid CFD Parallel Computation. *AIAA Journal of Aerospace Computing, Information, and Communication*, 5, No.11:2084–2091, 2008. doi: 10.2514/6.2007-4432.

[46] Y.-Q. Shen, G.-C. Zha, and B.-Y. Wang. Improvement of Stability and Accuracy of Implicit WENO Scheme . *AIAA Journal*, 47:331–344, 2009. doi: 10.2514/1.37697.

[47] B. McBreen, E. Butler, and G.-C. Zha. Analysis of Wall Jet Flow in EAPG with Super-Lift Coefficient. *AIAA 2024-0492, AIAA Scitech 2024 Forum. Orlando, FL, 8-12 Jan*, 2024. doi: 10.2514/6.2024-1406.

[48] Ren Y. Xu, K.-W. and G.-C. Zha. Flow Separation Control by CoFlow Wall Jet. *AIAA 2021-2946, AIAA Aviation 2021, Aug. 2-6*, 2021. doi: 10.2514/6.2021-2946.